ACS OMEGA

Open Access

http://pubs.acs.org/journal/acsodf

Article

Large-Gap $\mathbb{Z}_2$ and Topological Crystalline Insulating Phase in RbZnBi and CsZnBi

Hyunggeun Lee, Myung Joon Han,* and Kee Joo Chang*

Cite This: *ACS Omega* 2024, 9, 29820−29828

Read Online

ACCESS | Metrics & More | Article Recommendations

ABSTRACT: Topological insulators (TIs) are a new class of materials with gapless boundary states inside the bulk insulating gap. This metallic boundary state hosts intriguing phenomena such as helical spin textures and Dirac crossing points. Here, we theoretically propose RbZnBi and CsZnBi as a new family of TIs exhibiting large bulk band gaps and unique gapless surface states. Our first-principles density functional calculations show that two materials can be stabilized in two different structures depending on the stacking order of hexagonal ZnBi layers. While both materials in the AA-stacked structure become $\mathbb{Z}_2$ TI, the AB-stacked RbZnBi and CsZnBi are topological crystalline insulators with hourglass-shaped Fermion surface states protected by nonsymmorphic glide symmetry. The calculated bulk gap is about 1.5−1.8 times larger than that of Bi_2Se_3, which makes RbZnBi and CsZnBi promising candidates for future applications.

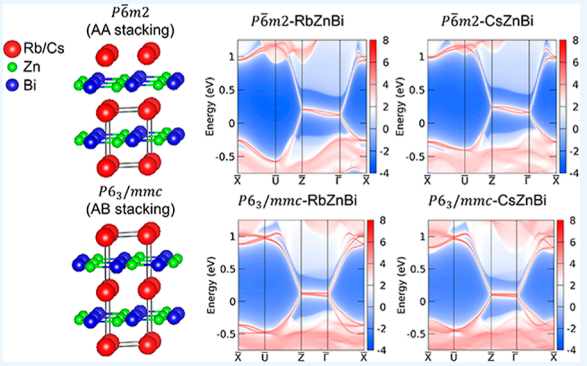

INTRODUCTION

The band structure of topological insulators (TIs) is characterized by a bulk insulating gap and a conducting edge or surface state at the boundary.[1,2] This nontrivial phase is a result of bulk band inversion caused by spin−orbit coupling (SOC). In the presence of time-reversal symmetry (TRS), conventional TIs are well classified in terms of $\mathbb{Z}_2$ invariants.[3,4] In $\mathbb{Z}_2$ TIs, TRS enforces the pair formation of gapless boundary states, which is topologically protected from scattering and gives rise to the Dirac points at time-reversal invariant momenta (TRIM). They are distinctive from TRS-broken Chern insulators, exhibiting a quantum anomalous Hall effect.[1,3−11] From the fact that the gapless boundary states host a unique helical spin texture and can carry dissipationless spin currents, TIs have been suggested to be useful for various applications, e.g., quantum computation and spintronic devices.[12,13] In spite of such remarkable potential, the practical applications at room temperature have been severely limited until now, largely owing to the small band gaps in real materials. For example, Bi_2Se_3 is arguably the most actively explored, and its band gap is ∼0.3 eV.[14−17] Therefore, searching for larger band gap $\mathbb{Z}_2$ TIs poses an important challenge and is indeed under active investigation.[18−29]

Unlike $\mathbb{Z}_2$ TIs, topological crystalline insulators (TCIs) have boundary states protected by crystal symmetry.[30] Their topological property should be characterized by another invariant, such as mirror Chern number C_M.[31] For example, SnTe is classified as a TCI with $C_M = -2$.[32,33] The surface Dirac point of TCIs can be located anywhere within the mirror invariant plane, i.e., not confined at the TRIM points. Recently proposed KHgSb is known to host a distinct type of surface Fermion states having an "hourglass"-shape dispersion due to the presence of additional nonsymmorphic symmetry.[34] This has been verified by angle-resolved photoemission spectroscopy.[35,36] While some other materials have been proposed to be TCIs, such as PbPo[37] and PbTe,[38] the small band gap problem is again an important limitation for applications here as well. For example, the bulk gap of a representative TCI, SnTe, is ∼0.2 eV.[39]

In this work, we suggest two materials, namely, RbZnBi and CsZnBi, as promising candidates for applications. Our density functional theory (DFT) total energy and phonon calculations show that they are well stabilized in the form of a layered honeycomb structure. While the most stable structure is $P6_3/mmc$ and $P\bar{6}m2$ for RbZnBi and CsZnBi, respectively, the energy difference between these two materials is sufficiently small as it is attributed only to the different stacking of honeycomb ZnBi layers. It is therefore expected that both RbZnBi and CsZnBi can be synthesized in both structural phases through the proper

Received: April 11, 2024
Revised: June 5, 2024
Accepted: June 7, 2024
Published: June 24, 2024

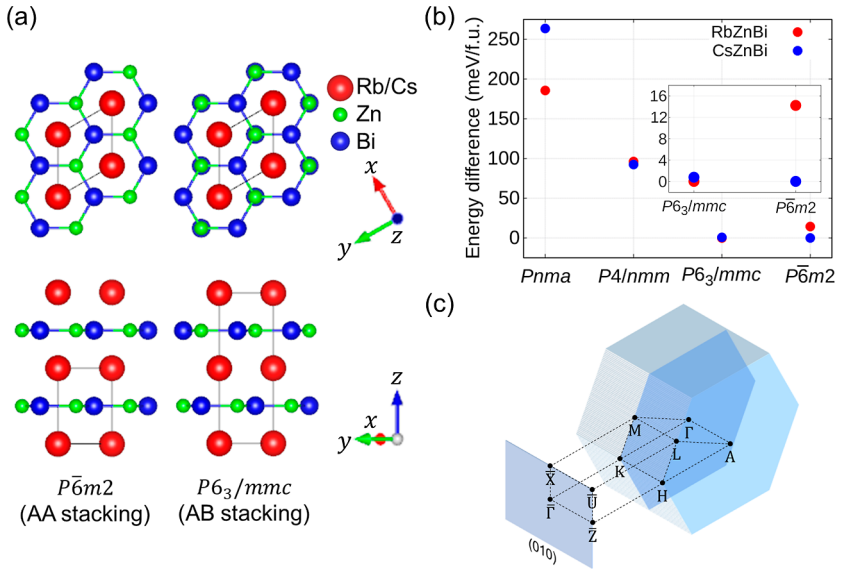

Figure 1. (a) Crystal structures of RbZnBi/CsZnBi with the space groups $P\bar{6}m2$ (left) and $P6_3/mmc$ (right), in which hexagonal ZnBi layers are stacked in AA and AB types, respectively. Red, green, and blue spheres represent Rb/Cs, Zn, and Bi atoms, respectively. (b) Calculated total energies of RbZnBi (red) and CsZnBi (blue) in the four different crystal structures *Pnma*, *P*4/*nmm*, $P6_3/mmc$, and $P\bar{6}m2$. The inset shows an enlarged view of the two most stable $P6_3/mmc$ and $P\bar{6}m2$. (c) Bulk and the (010) surface BZ with the labeled high-symmetry momenta.

control of experimental conditions. Our Wannier charge center (WCC) and surface state analyses clearly show that AA- and AB-stacked RbZnBi and CsZnBi become $\mathbb{Z}_2$ TI and TCI, respectively. In the AB-stacked structure, "hourglass fermion" surface states are identified as being protected by nonsymmorphic symmetry. Furthermore, the calculated bulk band gap is as large as 0.4−0.5 eV, which is 1.5−1.8 times greater than that of Bi_2Se_3. Considering the well-known feature of generalized gradient approximation (GGA) to underestimate the gap size, these two materials are promising new TIs for applications.

COMPUTATIONAL DETAILS

First-principles calculations were carried out within the DFT framework. We used GGA exchange−correlation functional by Perdew, Burke, and Ernzerhof (PBE)[40] as implemented in the Vienna Ab initio Simulation Package (VASP).[41,42] The wave functions were expanded in plane waves up to an energy cutoff of 500 eV, and Brillouin zone (BZ) integration was performed using a set of **k**-points with a grid spacing of $2\pi \times 0.12$ Å^{-1}. 12 ×12 × 8 and 12 × 12 × 4 Γ-centered **k**-point meshes were used for the $P\bar{6}m2$ and $P6_3/mmc$ crystal structure, respectively. The lattice geometry was fully optimized until the residual forces were less than 1 meV/Å. The (010) surface electronic structure was investigated with a $\sqrt{3} \times 1 \times 1$ supercell geometry for which 6 × 10 × 8 and 6 × 10 × 4 Γ-centered **k**-point meshes were used for the $P\bar{6}m2$ and $P6_3/mmc$ structures, respectively. For WCC calculations, we constructed maximally localized Wannier functions and a tight-binding Hamiltonian using the WANNIER90 code.[43] The surface electronic spectra were obtained using the iterative Green's function method[44] as implemented in the WannierTools code.[45]

RESULTS AND DISCUSSION

Crystal Structures of RbZnBi and CsZnBi. AZnX (A = Li, Na, K, Rb, Cs; X = Sb, Bi) Zintl compounds have attracted great interest due to their electronic properties[46−48] and potential applications to photovoltaics[49] and thermoelectrics.[50−52] They exhibit a variety of crystal structures that are highly dependent on the type of cation A. Li-based compounds have been synthesized in a hexagonal LiGaGe-type structure with the $P6_3mc$ space group,[53,54] whereas Na-based compounds crystallize in a tetragonal PbFCl structure with the space group *P*4/*nmm*.[55,56] As the cation A size increases, a hexagonal ZrBeSi-type structure (space group $P6_3/mmc$) is known to become more favorable. Examples include KZnSb,[55] KZnBi,[47] RbZnSb,[57] and CsZnSb.[57] In particular, $P6_3/mmc$ Zintl compounds have AB-stacked ZnX hexagonal layers with alkali metals embedded between the layers; see Figure 1a. The AA stacking Zintl phase is also reported in KZnSb, for example, which results in the $P\bar{6}m2$ structure shown in Figure 1a.[58]

Our proposed materials, RbZnBi and CsZnBi, have not been experimentally synthesized yet. Here, we explore their stability, crystal structure, and electronic properties. Four possible crystal structures are considered: *Pnma*, *P*4/*nmm*, $P6_3/mmc$, and $P\bar{6}m2$. The orthorhombic *Pnma* MgSrSi-type structure can be obtained by distorting the high-symmetry $P6_3/mmc$ structure,[59] as observed in NaCdX (X = Sb, Bi).[55,56] The DFT total energy calculation results are summarized in Figure 1b. The $P6_3/mmc$ and $P\bar{6}m2$ phases are found to be the most stable for RbZnBi and CsZnBi, respectively. Since these two structures differ only by the stacking order of ZnBi layers, the relative energy difference is small in both RbZnBi and CsZnBi; $|\Delta E| \sim 14.2$ and 0.8 meV/f.u. for RbZnBi and CsZnBi, respectively. See the inset of Figure 1b. We note that this is smaller than $|\Delta E| = 29.6$ meV/f.u. between $P6_3/mmc$- and $P\bar{6}m2$-KZnSb. Further results of the calculations to check stability can be found in Appendix A. Our results indicate that both structural phases can be synthesized in experiments by controlling synthesis conditions.

$\mathbb{Z}_2$ TI Phase in AA-Stacked RbZnBi and CsZnBi. The $P\bar{6}m2$ structure with an AA layer stacking is characterized by three important symmetries: A 3-fold rotation symmetry C_{3z} about the *z*-axis and two mirror symmetries, M_y: $(x,y,z) \rightarrow (x,-y,z)$ and M_z: $(x,y,z) \rightarrow (x,y,-z)$. Our calculations, including SOC, show that both RbZnBi and CsZnBi in this structure are semiconducting with a band gap of 0.53 and 0.48 eV,

https://doi.org/10.1021/acsomega.4c03506
ACS Omega 2024, 9, 29820−29828

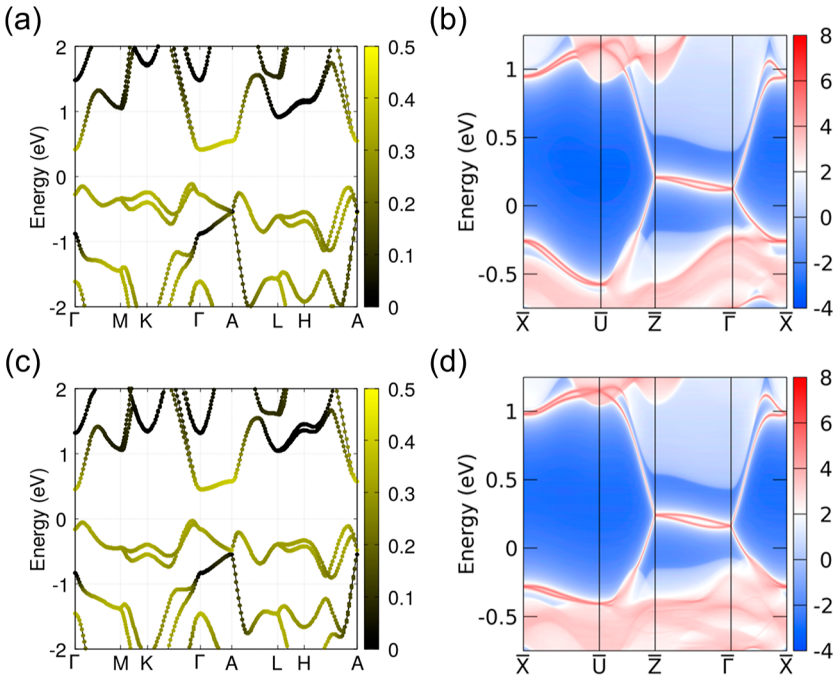

Figure 2. (a,c) Calculated bulk band dispersions of (a) RbZnBi and (c) CsZnBi in the AA-stacked $P\bar{6}m2$ structure. The color bar represents the degree of Bi-p orbital contribution to each eigenvalue. (b,d) Surface electronic structures of (b) RbZnBi and (d) CsZnBi projected onto the (010) surface.

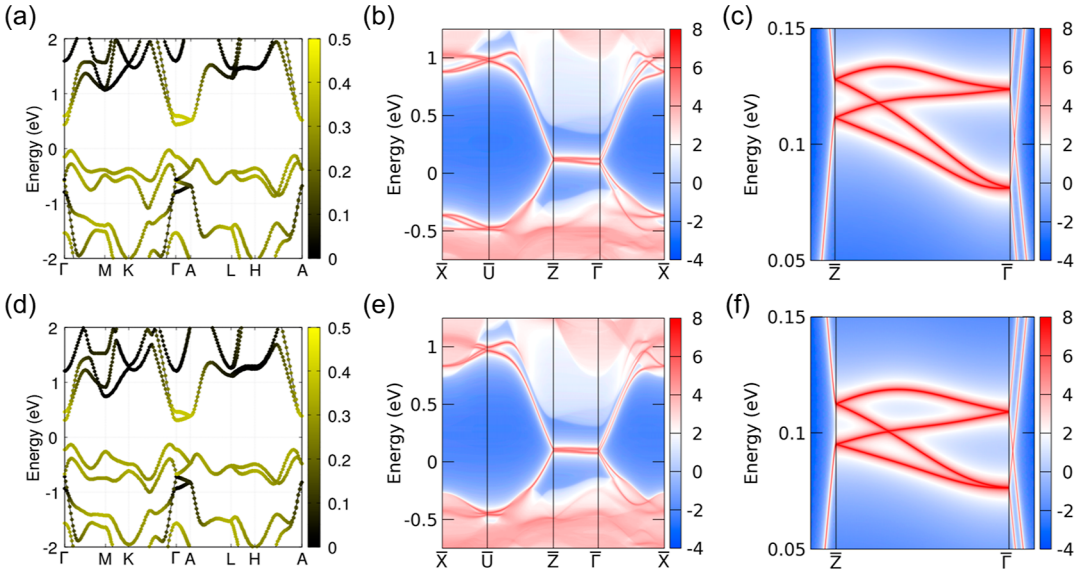

Figure 3. (a,d) Calculated bulk band structures of (a) RbZnBi and (d) CsZnBi in the $P6_3/mmc$ structure, including SOC. The color bar represents the Bi-p orbital contribution. (b,c,e,f) (010) surface electronic structures of (b,c) RbZnBi and (e,f) CsZnBi projected onto the (010) surface. Enlarged views of the hourglass Fermion surface states along $\bar{Z}$–$\bar{\Gamma}$ are presented in (c,f).

respectively. See Figure 2a,c, where 2-fold band degeneracy is clearly observed along the mirror invariant Γ−M and A−L lines as implied by the anticommutation relation between M_y and M_z. The calculation without SOC verifies that SOC is indispensable for band gap opening in both materials. Figure 2a,c also shows the orbital character of each band. Bi-p states (depicted in yellow) dominate the valence band region down to about −5 eV below the Fermi energy and also appear near the conduction band edge state along the Γ−A line. This can be indicative of the characteristic band inversion of the TI.

In order to clarify their band topology, we investigate WCCs on the six invariant planes, and the results are shown in Appendix B. It is clear that the WCC flow is nontrivial only in the two planes of $k_z = 0$ and $k_z = \pi/c$, indicating a weak TI with $(\nu_0; \nu_1\nu_2\nu_3) = (0; 001)$. This conclusion can be further verified by examining the surface states on the surfaces perpendicular to the (001) plane. Figure 2b,d presents our electronic structure calculations of the (010) surface. The well-identified features are the gapless surface states across the bulk band gap along the $\bar{U}$–$\bar{Z}$–$\bar{\Gamma}$–$\bar{X}$. While TRS enforces 2-fold band degeneracy at TRIM points, the Kramers partner exchange occurs in $\bar{U}$–$\bar{Z}$ as well as $\bar{\Gamma}$–$\bar{X}$. This typical feature of a two-dimensional TI is consistent with the result of $\mathbb{Z}_2$ indices obtained from WCC calculations.

https://doi.org/10.1021/acsomega.4c03506
ACS Omega 2024, 9, 29820−29828

We hereby conclude that $P\bar{6}m2$-structured RbZnBi and CsZnBi are weak $\mathbb{Z}_2$ TIs.

TCI Phase in AB-Stacked RbZnBi and CsZnBi. In contrast to $P\bar{6}m2$, the $P6_3/mmc$ structure has an inversion symmetry (P). While C_{3z} and M_y are still maintained, the M_z mirror symmetry is broken in $P6_3/mmc$. Instead, there are two nonsymmorphic glide symmetries: $\tilde{M}_x$: $(x, y, z) \rightarrow (-x, y, z + 1/2)$ and $\tilde{M}_z$: $(x, y, z) \rightarrow (x, y, -z + 1/2)$. In Figure 3a,d, we present the band structures of $P6_3/mmc$ RbZnbi and CsZnBi, respectively. As in the case of $P\bar{6}m2$, they are semiconducting, with sizable SOC-induced bulk gaps of 0.47 and 0.44 eV, respectively.

Just as in $P\bar{6}m2$, band inversion is clearly observed in Figure 3a,d. The (010) surface electronic structure also confirms the existence of gapless surface states, indicative of a TI; see Figure 3b,e. Unlike the AA-stacked structure, on the other hand, the $P6_3/mmc$ case exhibits unique hourglass Fermion dispersions along $\bar{Z}$–$\bar{\Gamma}$, as highlighted in Figure 3c,f. This unique surface state in $P6_3/mmc$-RbZnBi is in good agreement with the previous prediction.[60] Kramers partner exchange does not occur in $\bar{U}$–$\bar{Z}$, but it does in $\bar{\Gamma}$–$\bar{X}$. Also, it is clearly observed that two surface states go up along $\bar{X}$–$\bar{\Gamma}$–$\bar{X}$ and the other two down, crossing from the valence to the conduction band. This implies a Chern number of ±2 corresponding to each state. In fact, our WCC calculation for the $k_z = 0$ plane confirms that the mirror Chern number is 2; see Appendix C. This is consistent with the characteristic surface electronic structure, verifying that AB-stacked RbZnBi and CsZnBi are well-identified as TCIs.

The characteristic hourglass dispersion is attributed to TRS in combination with $\tilde{M}_x$. The eigenstates in the $\bar{Z}$–$\bar{\Gamma}$ line have eigenvalues of $\pm ie^{-ik_z c/2}$ for $\tilde{M}_x$. At the TRIM points $\bar{Z}$ and $\bar{\Gamma}$, the eigenvalues of the time-reversed (Θ) partner $\Theta|\psi_\pm(\mathbf{k})\rangle$ for $\tilde{M}_x$ can be obtained as follows

$$\begin{aligned}\tilde{M}_x(\Theta|\psi_\pm(\mathbf{k})\rangle) &= \Theta\tilde{M}_x|\psi_\pm(\mathbf{k})\rangle \\ &= \mp ie^{\frac{ik_z c}{2}}\Theta|\psi_\pm(\mathbf{k})\rangle,\end{aligned} \tag{1}$$

where we used the commutation relation $[\tilde{M}_x, \Theta] = 0$. Thus, the pairs sharing the same energy should have the same eigenvalues at $\bar{Z}$ (e.g., {+1,+1} or {−1,−1}), but at $\bar{\Gamma}$, they differ in their signs (e.g., {+i,−i}). Considering the continuity of the aforementioned eigenvalues for $\tilde{M}_x$, this constraint leads to the hourglass formation.

2-Fold surface band degeneracy along $\bar{U}$–$\bar{Z}$ is attributed to TRS and $\tilde{M}_x$ (see Figure 3b,e). This can be easily understood by introducing an effective time-reversal operator $\tilde{M}_x\Theta$ that satisfies $(\tilde{M}_x\Theta)^2 = e^{-ik_z c}$. As it becomes −1 at $k_z = \pi/c$, Kramers' theorem can be applied to $\tilde{M}_x\Theta$ and elucidates the 2-fold degeneracy.

Finally, it is also important to note the symmetry property along the A–L line. Figure 3a,d shows the 4-fold degeneracy along this line, whereas 2-fold band degeneracy is enforced in the other part of BZ by the coexistence of inversion P and Θ. As shown in the following, this is a consequence of four intercombined symmetries: P, Θ, M_y, and $\tilde{M}_z$. First of all, along A–L, the Hamiltonian $H(\mathbf{k})$ is invariant under not only the operation $I \equiv P\Theta$ (where Θ and P are applied sequentially) but also under $\tilde{M}_z$ and M_y. The eigenstate $|\psi(\mathbf{k})\rangle$ of Hamiltonian $H(\mathbf{k})$ can be labeled as $|\psi_\pm(\mathbf{k})\rangle$ with the eigenvalues $\pm i$ for $\tilde{M}_z$. In other words, $\tilde{M}_z|\psi_\pm(\mathbf{k})\rangle = \pm i|\psi_\pm(\mathbf{k})\rangle$. Now, we note that, along A–L

$$\begin{aligned}\tilde{M}_z(I|\psi_\pm(\mathbf{k})\rangle) &= e^{ik_z c}I\tilde{M}_z|\psi_\pm(\mathbf{k})\rangle \\ &= \mp ie^{ik_z c}I|\psi_\pm(\mathbf{k})\rangle,\end{aligned} \tag{2}$$

where $\tilde{M}_z P|\psi_\pm(\mathbf{k})\rangle = e^{-ik_z c}P\tilde{M}_z|\psi_\pm(\mathbf{k})\rangle$ is used. Namely, Kramers pairs share the same eigenvalues with $\tilde{M}_z$ at $k_z = \pi/c$. As for $M_y|\psi_\pm(\mathbf{k})\rangle$

$$\begin{aligned}\tilde{M}_z(M_y|\psi_\pm(\mathbf{k})\rangle) &= -M_y\tilde{M}_z|\psi_\pm(\mathbf{k})\rangle \\ &= \mp iM_y|\psi_\pm(\mathbf{k})\rangle.\end{aligned} \tag{3}$$

From the fact that a spin-1/2 system satisfies the anticommutation relation $\{\tilde{M}_z, M_y\} = 0$, $M_y|\psi_\pm(\mathbf{k})\rangle$ should have different eigenvalues from $\tilde{M}_z$. Also, the time-reversed partner of $M_y|\psi_\pm(\mathbf{k})\rangle$, $IM_y|\psi_\pm(\mathbf{k})\rangle$, has the eigenvalues $\pm ie^{ik_z c}$, which are the same as those of $M_y|\psi_\pm(\mathbf{k})\rangle$ at $k_z = \pi/c$. Given the Kramers' degeneracy theorem that Kramers pair states are orthogonal, these series of relations indicate that $M_y|\psi_\pm(\mathbf{k})\rangle$ are orthogonal to $|\psi_\pm(\mathbf{k})\rangle$ as well. As three operations, i.e., $\tilde{M}_z$, M_y, and I, are commutative with Hamiltonian $H(\mathbf{k})$, four orthogonal states $|\psi_\pm(\mathbf{k})\rangle$, $I|\psi_\pm(\mathbf{k})\rangle$, $M_y|\psi_\pm(\mathbf{k})\rangle$, and $IM_y|\psi_\pm(\mathbf{k})\rangle$ share the same energy in the A–L line.

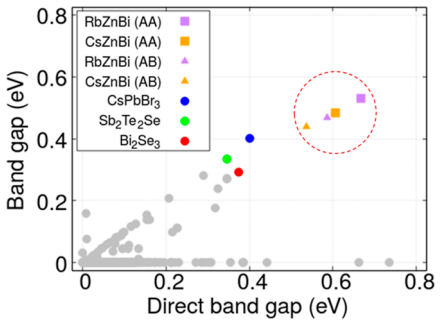

Figure 4. Calculated fundamental and direct band gaps of RbZnBi and CsZnBi in comparison to those of other topological materials in the "TopoMat" database.[61] Purple square, orange square, purple triangle, and orange triangle (in a red dashed circle) refer to the results of $P\bar{6}m2$-RbZnBi, $P\bar{6}m2$-CsZnBi, $P6_3/mmc$-RbZnBi, and $P6_3/mmc$-CsZnBi, respectively. The blue, green, and red circles show the gap of $CsPbBr_3$, Sb_2Te_2Se, and Bi_2Se_3, respectively. All other materials are represented by gray circles.

Discussion. From the point of view of practical applications, the small band gap of TIs is a serious obstacle, and therefore, searching for a large gap material has been an important research direction. Previous DFT calculations suggested some promising candidates, including BiC_2Br,[26] $PbCH_3$,[28] and $SrPoO_3$,[29] whose band gaps within GGA-PBE were predicted to be 0.99, 0.98, and 0.87 eV, respectively. Unfortunately, however, their experimental realization has not been reported yet. Our proposed materials, RbZnBi and CsZnBi, not only have a sizable bulk gap but also seem highly likely to be synthesized in both structures of AA- and AB-stacking. First, their energetic stability and dynamical stability are well supported by our computations (see Appendix A). Also, it is noted that KZnBi has already been synthesized in the same hexagonal structure of $P6_3/mmc$.[47] As for the band gap size, RbZnBi and CsZnBi show 150–180%

https://doi.org/10.1021/acsomega.4c03506
ACS Omega 2024, 9, 29820−29828

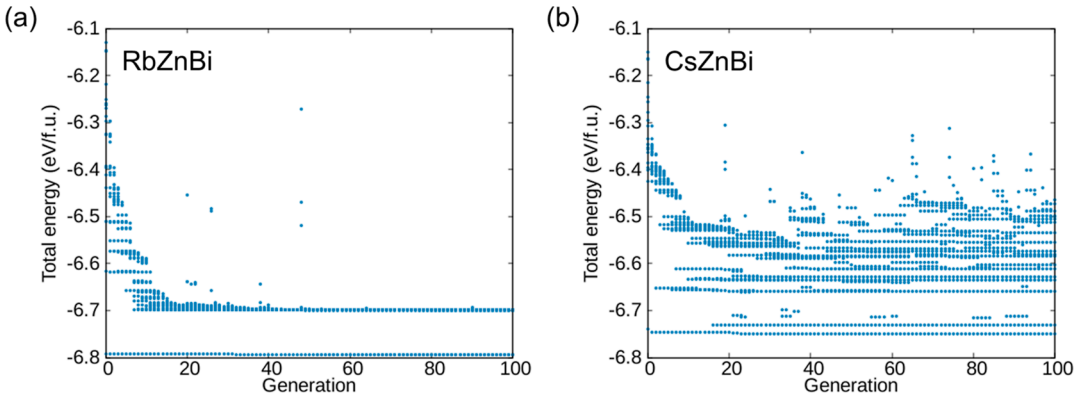

Figure A1. Total energy distribution of the configurations generated from *ab initio* evolutionary crystal structure search calculations: (a) RbZnBi and (b) CsZnBi. A total of 2000 configurations have been computed, and the AA-stacked hexagonal structure with $P\bar{6}m2$ is found to be the most stable structure for both RbZnBi and CsZnBi.

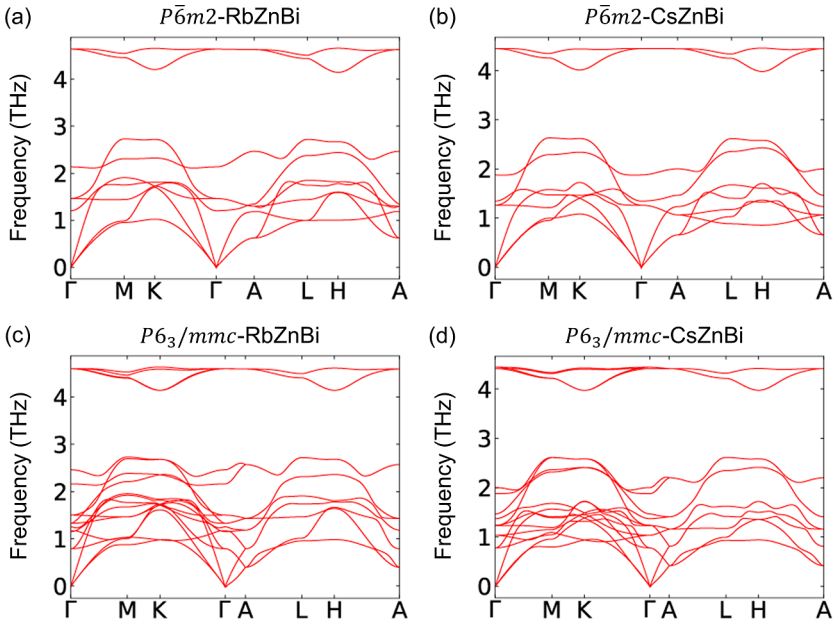

Figure A2. Calculated phonon dispersions of (a) $P\bar{6}m2$-RbZnBi, (b) $P\bar{6}m2$-CsZnBi, (c) $P6_3/mmc$-RbZnBi, and (d) $P6_3/mmc$-CsZnBi.

enhancement (within GGA-PBE) compared to Bi_2Se_3, which is arguably the most practical TI material at this moment. The gap size we report here is larger than those of 4050 known TIs in the "TopoMat" database;[61] see Figure 4. In addition, we point out that it is possible to design $\mathbb{Z}_2$ TIs by simply changing the stacking pattern in the layered structure of $P6_3/mmc$. In recent theoretical calculations,[60] several $\mathbb{Z}_2$ TI phases were reported for AB-stacked BMBi compounds (B = Na, K, Rb; M = Mg, Ca, Sr, Ba, Zn, Cd, Hg). Among these materials, NaCaBi was suggested as a $\mathbb{Z}_2$ TI with a band gap of 0.34 eV. We find that our proposed AA-stacked RbZnBi and CsZnBi are more attractive because they are $\mathbb{Z}_2$ TIs with larger band gaps than that of NaCaBi.

CONCLUSIONS

Based on first-principles DFT calculations, we suggest RbZnBi and CsZnBi as a new family of wide bulk gap topological materials. The results of total energy, phonon spectrum, and molecular dynamics (MD) simulation show their stability in $P\bar{6}m2$ and $P6_3/mmc$. The small energy difference between the two structures indicates that they can be synthesized in both forms by controlling the experimental conditions. Interestingly, the two different structures give rise to two different topological phases. In the $P\bar{6}m2$ structure with the AA-stacked hexagonal ZnBi layers, RbZnBi and CsZnBi become weak TIs with $(\nu_0; \nu_1\nu_2\nu_3) = (0; 001)$. In the AB-stacked $P6_3/mmc$, they become TCIs with hourglass surface states. The GGA-PBE bulk gap is as large as 0.48−0.53 and 0.44−0.47 eV for $P\bar{6}m2$ and $P6_3/mmc$. These values are about 1.5−1.8 times greater than that of Bi_2Se_3. The suggested new materials can be good candidate TIs for future device applications.

APPENDIX A

Stability of AA- and AB-stacked structures of RbZnBi and CsZnBi

To explore the stable crystal structures of RbZnBi and CsZnBi, we performed the crystal structure search calculations based on the evolutionary algorithm implemented in the AMADEUS code.[62] We considered a four-formula-unit cell and used 20 sampled populations for each generation. The crystal structure was fully optimized in each generation. We used an energy cutoff of 400 eV for the plane-wave expansion and a **k**-point mesh with

https://doi.org/10.1021/acsomega.4c03506
ACS Omega 2024, 9, 29820−29828

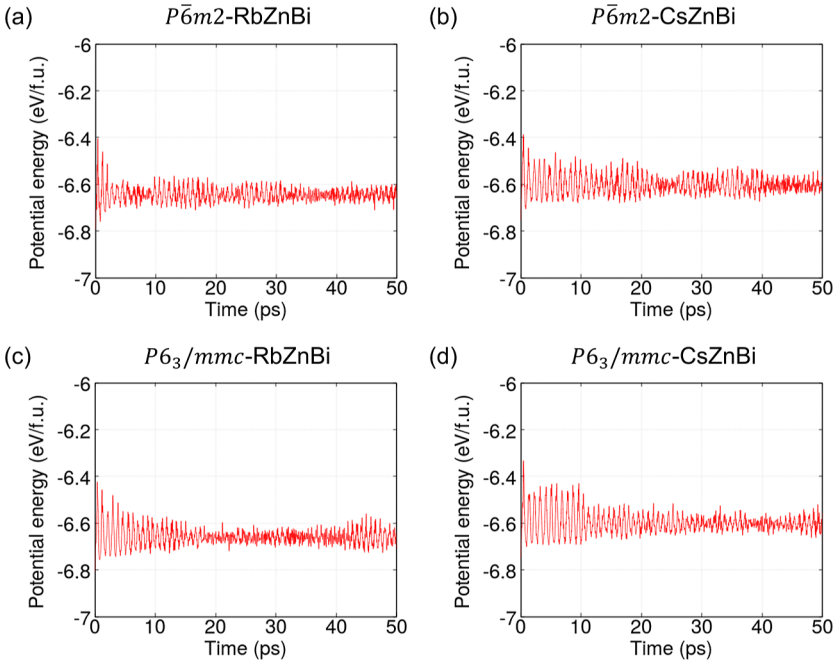

Figure A3. MD simulations at 400 K for (a) $P\bar{6}m2$-RbZnBi, (b) $P\bar{6}m2$-CsZnBi, (c) $P6_3/mmc$-RbZnBi, and (d) $P6_3/mmc$-CsZnBi.

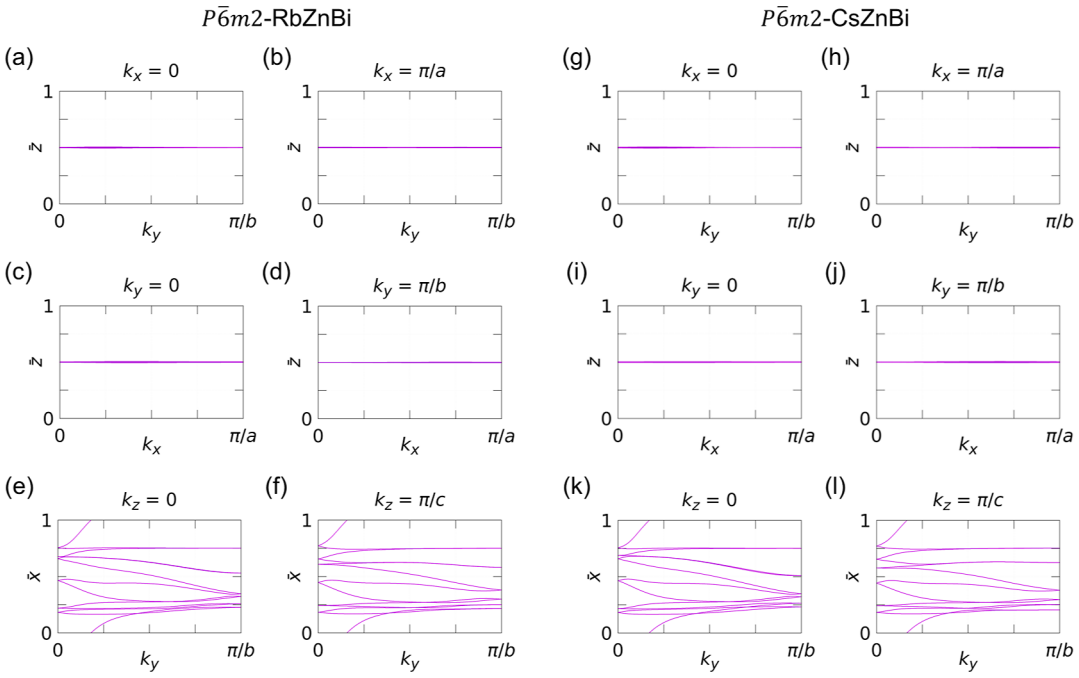

Figure A4. WCC evolutions in the AA-stacked (a–f) RbZnBi and (g–l) CsZnBi. A $\sqrt{3} \times 1 \times 1$ supercell geometry was used for the calculations.

a grid spacing of $2\pi \times 0.25$ Å^{-1}. This algorithmic search gives rise to the result that the AA-stacking $P\bar{6}m2$ phase is most stable for both RbZnBi and CsZnBi, as shown in Figure A1. However, we carried out more precise DFT calculations for the low-lying configurations and verified that, for the case of RbZnBi, the AB-stacked is lower in energy than the AA-stacked. $P6_3/mmc$ is slightly more stable with the energy difference of 14.2 meV per formula unit.

We also investigated the dynamical stability by calculating the phonon dispersion based on the finite displacement method implemented in the PHONOPY code.[63,64] The results are shown in Figure A2. No imaginary phonon mode is found over the whole BZ in both AA- and AB-stacked structures. To examine thermal stability, we performed *ab initio* MD simulations at 400 K. We used $2 \times 2 \times 2$ and $2 \times 2 \times 1$ supercells for $P\bar{6}m2$ and $P6_3/mmc$ structures, respectively. As shown in Figure A3, their crystal structures are well maintained.

APPENDIX B

$\mathbb{Z}_2$ indices of AA-stacked RbZnBi and CsZnBi

To determine the $\mathbb{Z}_2$ indices for AA-stacked RbZnBi and CsZnBi, we performed the WCC calculations for six different planes of $k_x = 0$, $k_x = \pi/a$, $k_y = 0$, $k_y = \pi/b$, $k_z = 0$, and $k_z = \pi/c$. As

https://doi.org/10.1021/acsomega.4c03506
ACS Omega 2024, 9, 29820−29828

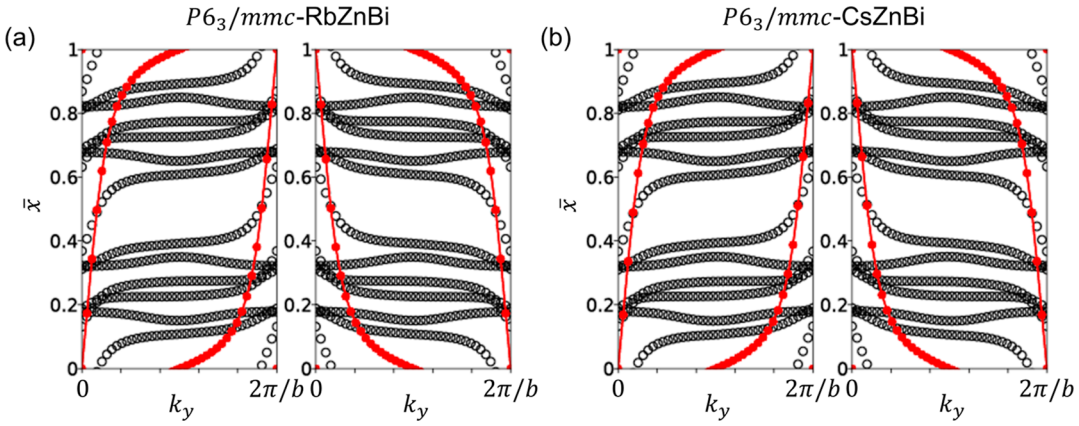

Figure A5. Flow of WCCs for AB-stacked $P6_3/mmc$ hexagonal (a) RbZnBi and (b) CsZnBi on the $k_z = 0$ plane. The WCCs (black dots) and their sum (red dots) for the $+i$ and $-i$ eigenstates for $\tilde{M}_z$ are shown in the left and right panels, respectively.

shown in Figure A4, an odd number of crossings (with respect to the horizontal reference line) are observed in the half BZ for $k_z = 0$ and $k_z = \pi/c$. For the other planes, even numbers of crossings are noticed. This indicates that only these two planes are topologically nontrivial. With the conventional $\mathbb{Z}_2$ indices, one can determine four independent three-dimensional topological invariants $(\nu_0; \nu_1\nu_2\nu_3) = (0; 001)$. RbZnBi and CsZnBi belong to the class of TRS-protected two-dimensional TIs.

APPENDIX C

Mirror Chern Numbers of AB-Stacked RbZnBi and CsZnBi

For AB-stacked RbZnBi and CsZnBi, the $\mathbb{Z}_2$ indices are found to be zero for all six planes of $k_x = 0$, $k_x = \pi/a$, $k_y = 0$, $k_y = \pi/b$, $k_z = 0$, and $k_z = \pi/c$. Paying attention to the nonsymmorphic glide symmetry $\tilde{M}_z$, we calculated the mirror Chern numbers. Here, we used Quantum ESPRESSO[65] and Z2Pack codes.[66] The $\sqrt{3} \times 1 \times 1$ supercell calculation was conducted with norm-conserving Vanderbilt pseudopotential, 50 Ry energy cutoff, and $6 \times 10 \times 4$ **k** mesh. Figure A5 shows the flow of WCCs (black) on the $k_z = 0$ plane and their sums (red) for the $+i$ and $-i$ eigenstates. It is clear that for both cases, Chern numbers $C_{\pm i}$ are nonzero. The mirror Chern number $C_M = (C_{+i} - C_{-i})/2 = +2$, which establishes that RbZnBi and CsZnBi in this structure are TCIs.

AUTHOR INFORMATION

Corresponding Authors

Myung Joon Han − *Department of Physics, Korea Advanced Institute of Science and Technology (KAIST), Daejeon 34141, Republic of Korea;* orcid.org/0000-0002-8089-7991; Email: mj.han@kaist.ac.kr

Kee Joo Chang − *Department of Physics, Korea Advanced Institute of Science and Technology (KAIST), Daejeon 34141, Republic of Korea;* orcid.org/0000-0002-5364-8551; Email: kjchang@kaist.ac.kr

Author

Hyunggeun Lee − *Department of Physics, Korea Advanced Institute of Science and Technology (KAIST), Daejeon 34141, Republic of Korea*

Complete contact information is available at: https://pubs.acs.org/10.1021/acsomega.4c03506

Notes

The authors declare no competing financial interest.

ACKNOWLEDGMENTS

This work was supported by the National Research Foundation of Korea (NRF) grant funded by the Korea government (MSIT) (no. 2021R1A2C1009303, no. 2018M3D1A1058754, and RS-2023-00253716).

REFERENCES

(1) Hasan, M. Z.; Kane, C. L. Colloquium: Topological insulators. *Rev. Mod. Phys.* **2010**, *82*, 3045−3067.

(2) Hasan, M. Z.; Moore, J. E. Three-Dimensional Topological Insulators. *Annu. Rev. Condens. Matter Phys.* **2011**, *2*, 55−78.

(3) Kane, C. L.; Mele, E. J. Z_2 Topological Order and the Quantum Spin Hall Effect. *Phys. Rev. Lett.* **2005**, *95*, 146802.

(4) Fu, L.; Kane, C. L. Time reversal polarization and a Z_2 adiabatic spin pump. *Phys. Rev. B: Condens. Matter Mater. Phys.* **2006**, *74*, 195312.

(5) Haldane, F. D. M. Model for a Quantum Hall Effect without Landau Levels: Condensed-Matter Realization of the "Parity Anomaly. *Phys. Rev. Lett.* **1988**, *61*, 2015−2018.

(6) Kane, C. L.; Mele, E. J. Quantum Spin Hall Effect in Graphene. *Phys. Rev. Lett.* **2005**, *95*, 226801.

(7) Chang, C.-Z.; Liu, C.-X.; MacDonald, A. H. Colloquium: Quantum anomalous Hall effect. *Rev. Mod. Phys.* **2023**, *95*, 011002.

(8) Li, P.; Li, X.; Zhao, W.; Chen, H.; Chen, M.-X.; Guo, Z.-X.; Feng, J.; Gong, X.-G.; MacDonald, A. H. Topological Dirac States beyond π-Orbitals for Silicene on SiC(0001) Surface. *Nano Lett.* **2017**, *17*, 6195−6202.

(9) Li, P.; Guo, Z.-X. The Dirac half-semimetal and quantum anomalous Hall effect in two-dimensional Janus $Mn_2X_3Y_3$ (X, Y = F, Cl, Br, I). *Phys. Chem. Chem. Phys.* **2021**, *23*, 19673−19679.

(10) Wang, K.; Li, Y.; Mei, H.; Li, P.; Guo, Z.-X. Quantum anomalous Hall and valley quantum anomalous Hall effects in two-dimensional d^0 orbital *XY* monolayers. *Phys. Rev. Mater.* **2022**, *6*, 044202.

(11) Li, P.; Yang, X.; Jiang, Q.-S.; Wu, Y.-Z.; Xun, W. Built-in electric field and strain tunable valley-related multiple topological phase transitions in $VSiXN_4$(X = C, Si, Ge, Sn, Pb) monolayers. *Phys. Rev. Mater.* **2023**, *7*, 064002.

(12) Wang, K. L.; Kou, X.; Upadhyaya, P.; Fan, Y.; Shao, Q.; Yu, G.; Amiri, P. K. Electric-Field Control of Spin-Orbit Interaction for Low-Power Spintronics. *Proc. IEEE* **2016**, *104*, 1974−2008.

(13) He, M.; Sun, H.; He, Q. L. Topological insulator: Spintronics and quantum computations. *Front. Phys.* **2019**, *14*, 43401.

(14) Xia, Y.; Qian, D.; Hsieh, D.; Wray, L.; Pal, A.; Lin, H.; Bansil, A.; Grauer, D.; Hor, Y. S.; Cava, R. J.; Hasan, M. Z. Observation of a large-gap topological-insulator class with a single Dirac cone on the surface. *Nat. Phys.* **2009**, *5*, 398−402.

(15) Dc, M.; Chen, J.-Y.; Peterson, T.; Sahu, P.; Ma, B.; Mousavi, N.; Harjani, R.; Wang, J.-P. Observation of High Spin-to-Charge Conversion by Sputtered Bismuth Selenide Thin Films at Room Temperature. *Nano Lett.* **2019**, *19*, 4836−4844.
(16) Park, H.; Jeong, K.; Maeng, I.; Sim, K. I.; Pathak, S.; Kim, J.; Hong, S.-B.; Jung, T. S.; Kang, C.; Kim, J. H.; Hong, J.; Cho, M.-H. Enhanced Spin-to-Charge Conversion Efficiency in Ultrathin Bi_2Se_3 Observed by Spintronic Terahertz Spectroscopy. *ACS Appl. Mater. Interfaces* **2021**, *13*, 23153−23160.
(17) Zhang, K.; Zhu, X.; Yang, Y.; Zhu, H. Polarization of Bi_2Se_3 thin film toward non-volatile memory applications. *AIP Adv.* **2022**, *12*, 085104.
(18) Xu, Y.; Yan, B.; Zhang, H.-J.; Wang, J.; Xu, G.; Tang, P.; Duan, W.; Zhang, S.-C. Large-Gap Quantum Spin Hall Insulators in Tin Films. *Phys. Rev. Lett.* **2013**, *111*, 136804.
(19) Kou, L.; Yan, B.; Hu, F.; Wu, S.-C.; Wehling, T. O.; Felser, C.; Chen, C.; Frauenheim, T. Graphene-Based Topological Insulator with an Intrinsic Bulk Band Gap above Room Temperature. *Nano Lett.* **2013**, *13*, 6251−6255.
(20) Niu, C.; Bihlmayer, G.; Zhang, H.; Wortmann, D.; Blügel, S.; Mokrousov, Y. Functionalized bismuth films: Giant gap quantum spin Hall and valley-polarized quantum anomalous Hall states. *Phys. Rev. B: Condens. Matter Mater. Phys.* **2015**, *91*, 041303.
(21) Hsu, C.-H.; Huang, Z.-Q.; Chuang, F.-C.; Kuo, C.-C.; Liu, Y.-T.; Lin, H.; Bansil, A. The nontrivial electronic structure of Bi/Sb honeycombs on SiC(0001). *New J. Phys.* **2015**, *17*, 025005.
(22) Pham, A.; Gil, C. J.; Smith, S. C.; Li, S. Orbital engineering of two-dimensional materials with hydrogenation: A realization of giant gap and strongly correlated topological insulators. *Phys. Rev. B: Condens. Matter Mater. Phys.* **2015**, *92*, 035427.
(23) Zhang, R.-w.; Zhang, C.-w.; Ji, W.-x.; Li, S.-s.; Yan, S.-s.; Li, P.; Wang, P.-j. Functionalized Thallium Antimony Films as Excellent Candidates for Large-Gap Quantum Spin Hall Insulator. *Sci. Rep.* **2016**, *6*, 21351.
(24) Padilha, J. E.; Pontes, R. B.; Schmidt, T. M.; Miwa, R. H.; Fazzio, A. A new class of large band gap quantum spin hall insulators: 2D fluorinated group-IV binary compounds. *Sci. Rep.* **2016**, *6*, 26123.
(25) Wang, D.; Chen, L.; Shi, C.; Wang, X.; Cui, G.; Zhang, P.; Chen, Y. Quantum spin Hall insulator in halogenated arsenene films with sizable energy gaps. *Sci. Rep.* **2016**, *6*, 28487.
(26) Wu, L.; Gu, K.; Li, Q. New families of large band gap 2D topological insulators in ethynyl-derivative functionalized compounds. *Appl. Surf. Sci.* **2019**, *484*, 1208−1213.
(27) Shvets, I. A.; Klimovskikh, I. I.; Aliev, Z. S.; Babanly, M. B.; Zúñiga, F. J.; Sánchez-Barriga, J.; Krivenkov, M.; Shikin, A. M.; Chulkov, E. V. Surface electronic structure of the wide band gap topological insulator $PbBi_4Te_4Se_3$. *Phys. Rev. B* **2019**, *100*, 195127.
(28) Mahmud, S.; Alam, M. K. Large bandgap quantum spin Hall insulator in methyl decorated plumbene monolayer: a first-principles study. *RSC Adv.* **2019**, *9*, 42194−42203.
(29) Lee, C.-H.; Tung, J.-C. Large Bandgap Topological Insulator in Oxide $APoO_3$ (A = Be, Mg, Ca, Sr, Ba, and Ra) Perovskite: An Ab Initio Study. *Appl. Sci.* **2021**, *11*, 1143.
(30) Fu, L. Topological Crystalline Insulators. *Phys. Rev. Lett.* **2011**, *106*, 106802.
(31) Teo, J. C. Y.; Fu, L.; Kane, C. L. Surface states and topological invariants in three-dimensional topological insulators: Application to $Bi_{1-x}Sb_x$. *Phys. Rev. B: Condens. Matter Mater. Phys.* **2008**, *78*, 045426.
(32) Hsieh, T. H.; Lin, H.; Liu, J.; Duan, W.; Bansil, A.; Fu, L. Topological crystalline insulators in the SnTe material class. *Nat. Commun.* **2012**, *3*, 982.
(33) Tanaka, Y.; Ren, Z.; Sato, T.; Nakayama, K.; Souma, S.; Takahashi, T.; Segawa, K.; Ando, Y. Experimental realization of a topological crystalline insulator in SnTe. *Nat. Phys.* **2012**, *8*, 800−803.
(34) Wang, Z.; Alexandradinata, A.; Cava, R. J.; Bernevig, B. A. Hourglass fermions. *Nature* **2016**, *532*, 189−194.
(35) Ma, J.; Yi, C.; Lv, B.; Wang, Z.; Nie, S.; Wang, L.; Kong, L.; Huang, Y.; Richard, P.; Zhang, P.; et al. Experimental evidence of hourglass fermion in the candidate nonsymmorphic topological insulator KHgSb. *Sci. Adv.* **2017**, *3*, No. e1602415.
(36) Liang, A. J.; Jiang, J.; Wang, M. X.; Sun, Y.; Kumar, N.; Shekhar, C.; Chen, C.; Peng, H.; Wang, C. W.; Xu, X.; et al. Observation of the topological surface state in the nonsymmorphic topological insulator KHgSb. *Phys. Rev. B* **2017**, *96*, 165143.
(37) Wang, Y.-p.; Ji, W.-x.; Zhang, C.-w.; Li, P.; Wang, P.-j. A new topological crystalline insulator in two-dimensional PbPo with tunable large bulk gaps. *J. Mater. Chem. C* **2016**, *4*, 8745−8749.
(38) Jia, Y.-z.; Ji, W.-x.; Zhang, C.-w.; Li, P.; Zhang, S.-f.; Wang, P.-j.; Li, S.-s.; Yan, S.-s. Prediction of topological crystalline insulators and topological phase transitions in two-dimensional PbTe films. *Phys. Chem. Chem. Phys.* **2017**, *19*, 29647−29652.
(39) Dimmock, J. O.; Melngailis, I.; Strauss, A. J. Band Structure and Laser Action in $Pb_xSn_{1-x}Te$. *Phys. Rev. Lett.* **1966**, *16*, 1193−1196.
(40) Perdew, J. P.; Burke, K.; Ernzerhof, M. Generalized Gradient Approximation Made Simple. *Phys. Rev. Lett.* **1996**, *77*, 3865−3868.
(41) Kresse, G.; Furthmüller, J. Efficiency of ab-initio total energy calculations for metals and semiconductors using a plane-wave basis set. *Comput. Mater. Sci.* **1996**, *6*, 15−50.
(42) Kresse, G.; Furthmüller, J. Efficient iterative schemes for ab initio total-energy calculations using a plane-wave basis set. *Phys. Rev. B: Condens. Matter Mater. Phys.* **1996**, *54*, 11169−11186.
(43) Pizzi, G.; Vitale, V.; Arita, R.; Blügel, S.; Freimuth, F.; Géranton, G.; Gibertini, M.; Gresch, D.; Johnson, C.; Koretsune, T.; et al. Wannier90 as a community code: new features and applications. *J. Phys.: Condens. Matter* **2020**, *32*, 165902.
(44) Sancho, M. P. L.; Sancho, J. M. L.; Sancho, J. M. L.; Rubio, J. Highly convergent schemes for the calculation of bulk and surface Green functions. *J. Phys. F: Met. Phys.* **1985**, *15*, 851−858.
(45) Wu, Q.; Zhang, S.; Song, H.-F.; Troyer, M.; Soluyanov, A. A. WannierTools: An open-source software package for novel topological materials. *Comput. Phys. Commun.* **2018**, *224*, 405−416.
(46) Cao, W.; Tang, P.; Xu, Y.; Wu, J.; Gu, B.-L.; Duan, W. Dirac semimetal phase in hexagonal LiZnBi. *Phys. Rev. B* **2017**, *96*, 115203.
(47) Song, J.; Kim, S.; Kim, Y.; Fu, H.; Koo, J.; Wang, Z.; Lee, G.; Lee, J.; Oh, S. H.; Bang, J.; et al. Coexistence of Surface Superconducting and Three-Dimensional Topological Dirac States in Semimetal KZnBi. *Phys. Rev. X* **2021**, *11*, 021065.
(48) Lee, H.; Kang, Y.-G.; Jung, M.-C.; Han, M. J.; Chang, K. J. Robust dual topological insulator phase in NaZnBi. *NPG Asia Mater.* **2022**, *14*, 36.
(49) Reshak, A. H. Nowotny−Juza NaZnX (X = P, As and Sb) as photovoltaic materials. *Sol. Energy* **2015**, *115*, 430−440.
(50) Madsen, G. K. H. Automated Search for New Thermoelectric Materials: The Case of LiZnSb. *J. Am. Chem. Soc.* **2006**, *128*, 12140−12146.
(51) White, M. A.; Miller, G. J.; Vela, J. Polytypism and Unique Site Preference in LiZnSb: A Superior Thermoelectric Reveals Its True Colors. *J. Am. Chem. Soc.* **2016**, *138*, 14574−14577.
(52) Haque, E. First-principles predictions of low lattice thermal conductivity and high thermoelectric performance of AZnSb (A = Rb, Cs). *RSC Adv.* **2021**, *11*, 15486−15496.
(53) Schroeder, G.; Schuster, H.-U. Notizen: LiZnSb, eine weitere ternäre Phase mit Wurtzitgerüst/LiZnSb, an Additional Ternary Phase with a Wurtzit-type Lattice. *Z. Naturforsch., B: Anorg. Chem., Org. Chem.* **1975**, *30*, 978−979.
(54) Tiburtius, C.; Schuster, H.-U. LiBeSb und LiZnBi, ternäre Verbindungen mit Wurtzitgerüst/LiBeSb and LiZnBi, Ternary Compounds with a Wurtzit-type Lattice. *Z. Naturforsch., B: Anorg. Chem., Org. Chem.* **1978**, *33*, 35−38.
(55) Savelsberg, G. Ternäre Pnictide und Chalkogenide von Alkalimetallen und IB-bzw. IIB-Elementen/On Ternary Pnictides and Chalkogenides of Alkaline Metals and IB-resp. II B-Elements. *Z. Naturforsch., B: Anorg. Chem., Org. Chem.* **1978**, *33*, 370−373.
(56) Shilov, A. I.; Pervakov, K. S.; Tafeenko, V. A.; Morozov, I. V. New Ternary Bismuthides NaZnBi and NaCdBi: Synthesis and Crystal Structures. *Russ. J. Coord. Chem.* **2020**, *46*, 622−630.

https://doi.org/10.1021/acsomega.4c03506
ACS Omega 2024, 9, 29820−29828

(57) Owens-Baird, B.; Wang, L.-L.; Lee, S.; Kovnir, K. Synthesis, Crystal and Electronic Structure of Layered AMSb Compounds (A = Rb, Cs; M = Zn, Cd). *Z. fur Anorg. Allg. Chem.* **2020**, *646*, 1079−1085.
(58) Kahlert, H.; Schuster, H.-U. Notizen: Elektrovalente temarnäre Phasen des Natriums bzw. Kaliums mit 2 B- und 5 B-Elementen/ Ternary Phases of Sodium or Potassium with Elements of the 2 b- and 5 b-Group. *Z. Naturforsch., B: Anorg. Chem., Org. Chem.* **1976**, *31*, 1538−1539.
(59) Bennett, J. W.; Garrity, K. F.; Rabe, K. M.; Vanderbilt, D. Orthorhombic *ABC* Semiconductors as Antiferroelectrics. *Phys. Rev. Lett.* **2013**, *110*, 017603.
(60) Shao, D.; Guo, Z.; Wu, X.; Nie, S.; Sun, J.; Weng, H.; Wang, Z. Topological insulators in the NaCaBi family with large spin-orbit coupling gaps. *Phys. Rev. Res.* **2021**, *3*, 013278.
(61) Autès, G.; Wu, Q.; Mounet, N.; Yazyev, O. V. *TopoMat: a database of high-throughput first-principles calculations of topological materials*, 2019.
(62) Lee, I.-H.; Oh, Y. J.; Kim, S.; Lee, J.; Chang, K. J. Ab initio materials design using conformational space annealing and its application to searching for direct band gap silicon crystals. *Comput. Phys. Commun.* **2016**, *203*, 110−121.
(63) Togo, A. First-principles Phonon Calculations with Phonopy and Phono3py. *J. Phys. Soc. Jpn.* **2023**, *92*, 012001.
(64) Togo, A.; Chaput, L.; Tadano, T.; Tanaka, I. Implementation strategies in phonopy and phono3py. *J. Phys.: Condens. Matter* **2023**, *35*, 353001.
(65) Giannozzi, P.; Baroni, S.; Bonini, N.; Calandra, M.; Car, R.; Cavazzoni, C.; Ceresoli, D.; Chiarotti, G. L.; Cococcioni, M.; Dabo, I.; et al. QUANTUM ESPRESSO: a modular and open-source software project for quantum simulations of materials. *J. Phys.: Condens. Matter* **2009**, *21*, 395502.
(66) Gresch, D.; Autès, G.; Yazyev, O. V.; Troyer, M.; Vanderbilt, D.; Bernevig, B. A.; Soluyanov, A. A. Z2Pack: Numerical implementation of hybrid Wannier centers for identifying topological materials. *Phys. Rev. B* **2017**, *95*, 075146.

https://doi.org/10.1021/acsomega.4c03506
ACS Omega 2024, 9, 29820−29828